

# Structure and Thermodynamic Stability of Zeolitic Imidazolate Framework Surfaces

Tingting Weng and J.R. Schmidt\*

*Theoretical Chemistry Institute and Department of Chemistry, University of  
Wisconsin–Madison, Madison, Wisconsin, 53706, United States*

E-mail: [schmidt@chem.wisc.edu](mailto:schmidt@chem.wisc.edu)

## Abstract

Extensive efforts over the last several decades have focused on the possibility of “crystal engineering” metal-organic framework (MOF) materials with bulk properties tailored toward specific applications. However, beyond their bulk structure, MOF interfaces and surfaces can also play an important role in governing the materials properties relevant to many applications, including both interfacial mass and/or charge transport. We presently examine the diversity of stable surface structures / terminations of zeolitic imidazolate frameworks (ZIFs), a sub-class of MOFs, under a variety of conditions that are characteristic of either gas-phase, “post-synthetic” conditions (relevant to many MOF applications) or solution-phase conditions (typical of those used during MOF synthesis). We construct surface phase diagrams to predict the most stable ZIF surface terminations as a function of external parameters (including temperature, adsorbate pressures, and pH), making explicit comparison against prior experimental observations, when possible. We find that the resulting phase diagrams can be used to explain the results of prior experimental studies of ZIF terminations across a variety of conditions and provide important insights into the factors that govern the structure of ZIF interfaces.

## Introduction

The synthesis of metal organic frameworks (MOFs) has attracted significant research focus over the past two decades due to the possibility of “crystal engineering” MOFs with specific structures and/or properties tailored toward myriad possible applications,<sup>1-3</sup> including gas storage,<sup>4,5</sup> separation<sup>6,7</sup> catalysis,<sup>8,9</sup> chemical sensing<sup>10</sup> and drug delivery.<sup>11,12</sup> As such, there is a now vast literature devoted to the examination of the relationship between a MOF’s structure and its associated bulk properties (e.g. surface area, adsorption isotherms).<sup>13</sup> However, it is becoming increasingly clear that, beyond this bulk structure, MOF surfaces and

interfaces play a vital role in governing both their synthesis (e.g. crystallization)<sup>14</sup> and in many of their practical applications (e.g. mass transport, conductivity, surface catalysis).<sup>15–19</sup> Nonetheless, detailed studies regarding MOF interfaces have only begun to appear relatively recently, and there remain substantial gaps in our present knowledge regarding the structure and relative thermodynamic stability of MOF surfaces.

Herein we focus specifically on zeolitic imidazolate frameworks (ZIFs), a sub-class of MOFs composed of  $\text{Zn}^{2+}$  cations coordinated via bridging imidazolate-based ligands. ZIFs are often observed to exhibit high chemical and thermal stability,<sup>20</sup> which, in addition to their intrinsic nano-porosity, yields many exciting applications.<sup>21,22</sup> ZIF-8 is a prototypical ZIF with sodalite (SOD) topology and 2-methylimidazolate (mim) linkers that has been the subject of numerous syntheses and characterization studies, including those focused in its interfacial structure. In many cases, these studies appear to present conflicting result for the ZIF surface termination, perhaps due to differences in the ZIF synthesis (e.g. room temperature vs. solvothermal, aqueous vs. organic solvent) or characterization conditions. Using in situ AFM, Moh et al. monitored the growth of ZIF-8 under solvothermal condition. They performed step height analysis of the resulting AFM deflection images, identifying a  $[\text{Zn}(\text{mim})_3]^-$  surface termination motif and the presence of nonframework species on the surface.<sup>23</sup> Tian et al. utilized X-ray photoelectron spectroscopy (XPS) to identify the involvement of carbonates, water/hydroxides, uncoordinated amines and mim in the termination of a ZIF-8 thin film under ultrahigh vacuum; those authors explained the presence of carbonates via exposure to ambient  $\text{CO}_2$  from air.<sup>24</sup> A high-resolution TEM (HRTEM) study by Zhu et al. revealed an ‘armchair’-type termination involving 2-methylimidazole (Hmim) capping of ZIF-8 (110) surfaces during crystal self-assembly.<sup>25</sup>

Corresponding computational studies of ZIF-8 surface structures/terminations are also scarce. Chizallet et al. demonstrated the existence of both acidic ( $\text{Zn}^{2+}$ ) and basic ( $\text{N}^-$  moieties and OH groups) sites at the external surfaces of ZIF-8 via CO adsorption using

density functional theory (DFT) calculations in conjunction with Fourier transform infrared (FTIR) spectroscopy.<sup>26</sup> Sholl and coworkers computed surface energies of various possible ZIF-8 facets ( $\{110\}$  and  $\{100\}$ ), but they did not attempt to discern the most stable terminations as a function of external conditions.<sup>27</sup> Later, using combination of DFT and molecular dynamics, Semino et al. modeled a ZIF-8/polymer interface and also examined several possible ZIF terminations.<sup>28</sup> Finally, a density-functional-based tight-binding (DFTB) examination of ZIF surfaces was conducted by Zhu et al.. Their calculated surface energies were used to support an 'armchair'-type surface termination, consistent with a prior HRTEM study.<sup>25</sup> Note that, in all these cases, the computational analysis of the ZIF terminations focused on energies (vs. free energies) and thus cannot be utilized to make predictions about the thermodynamically stable surface termination under varying conditions of temperature, linker/adsorbate concentrations or solution pH. Chizallet and Bats investigated various external ZIF surface sites with different Zn coordination number and their stability as a function of temperature and adsorbate ( $\text{H}_2\text{O}$  and  $\text{CO}_2$ ) pressure, using a finite cluster model for the ZIF surface. However, such a gas-phase model cannot account for the role of solvent during the synthesis process, solution pH, nor the concentration of the linker group. In contrast, the goal of the present work is to perform a computational analysis of the surface structure(s) and thermodynamic stability of ZIF interfaces under a wide range of synthetic and post-synthetic conditions.

Ultimately, the surface structure and termination of ZIF crystallites is controlled by a combination of thermodynamic and kinetic factors. Nonetheless, the relative thermodynamic stability of various ZIF terminations is ultimately governed by their relative surface free energies. Herein we utilize these surface (free) energies to generate a surface phase diagram, which determines the surface termination of ZIFs under thermodynamic control. Such phase diagrams play a key role in predicting the observed surface structure, particularly during high-temperature synthesis or after prolonged reaction times. Briefly, we first build ZIF

surface models consisting of various possible terminations, using DFT to calculate their surface free energies in vacuum. We then utilize molecular dynamics (MD) simulations in the presence of explicit solvent to calculate solvation effects, where appropriate, yielding results that are relevant to both synthetic and post-synthetic conditions. The resulting phase diagrams provide a consistent framework that can be used to explain the results of prior experimental studies of ZIF terminations across a variety of conditions and provides important insights into the factors governing the structure of ZIF interfaces.

## Methods

In this section, we detail our methodology for calculating the surface free energies of various ZIF surfaces and surface terminations under a variety of experimentally-relevant conditions; these surface energies in turn enable the construction of a ZIF surface phase diagram, dictating the thermodynamically most stable ZIF termination as a function of the relevant external parameters (e.g. temperature, pressure). We focus specifically on the (110) facet of ZIF-8, due to the prevalence of this facet in common rhombic dodecahedron crystals and the availability for corresponding characterization data (including HRTEM, AFM and XPS);<sup>23,25,27,30</sup> note that this surface contains only a single, low-energy cut that consists with cleaving the weak Zn-Im coordination bonds. In the construction of these phase diagrams, we account for the influence of temperature, adsorbate pressures / concentrations (solvent and/or Hmim) and, in solution, pH. We focus on two important regimes: post-synthetic conditions, i.e. under vacuum or humid air; and synthetic conditions, i.e. under solvent exposure (typically water or dimethylformamide [DMF]), potentially with excess Hmim.

## Surface Free Energy

The thermodynamically most stable surface (i.e. the facet, or specific termination thereof) is the one that minimizes the surface free energy,  $\gamma(T, p)$ ,<sup>31</sup> where

$$\gamma(T, p) = \frac{1}{2A} \left( G_{slab}(T, p, \{N_i\}) - \sum N_i \mu_i(T, p) \right) \quad (1)$$

and  $G_{slab}$  denotes the Gibbs free energy of a surface “slab” with total surface area of  $2A$ ,  $N_i$  is the amount of component  $i$  contained in (or adsorbed on) the slab, and  $\mu_i$  is the chemical potential of component  $i$  at temperature  $T$  and pressure  $p$ . In words, Eq. (1) denotes the free energy change per unit area for generating a surface from the bulk, accounting for possible surface adsorption of additional species from a reservoir (either the air or solution).

Using Eq. (1), we construct surface phase diagrams by plotting the surface free energy of various surface terminations as a function of the temperature, pressure, and/or adsorbate chemical potentials, with the equilibrium surface given by the one with the lowest surface free energy.<sup>32</sup> This general framework has been successfully utilized in a wide variety of contexts, including the studies of the surfaces of alloys,<sup>33</sup> semiconductors<sup>34–37</sup> and metal oxides;<sup>38–41</sup> we presently apply it to the examination of ZIFs.

## Surface Phase Diagrams in Gas Phase

For the gas phase, we consider a ZIF-8 (110) slab in equilibrium with an atmosphere of gaseous water and Hmim. (Note that we have not explicitly considered adsorption of  $\text{CO}_2$  which, along with water, is an important component of ambient air and could be important in some regimes, although likely not for three-coordinate Zn atoms that dominate the surface of large ZIF crystallites.<sup>29</sup>) The surface free energy,  $\gamma$ , is given by:

$$\begin{aligned}
\gamma &= \frac{1}{2A} \left( G_{Slab} - N_{Zn} \mu_{Bulk}^{Zn(mim)_2} - N_{Hmim} \mu_{Hmim} - N_{H_2O} \mu_{H_2O} \right) \\
&= \frac{1}{2A} \left[ \left( G_{Slab} - N_{Zn} \mu_{Bulk}^{Zn(mim)_2} - N_{Hmim} \mu_{Hmim}^{\ominus} - N_{H_2O} \mu_{H_2O}^{\ominus} \right) \right. \\
&\quad \left. - N_{Hmim} \Delta \mu_{Hmim} - N_{H_2O} \Delta \mu_{H_2O} \right] \tag{2}
\end{aligned}$$

Here  $\mu_{Bulk}^{Zn(mim)_2}$  is the bulk Gibbs free energy of ZIF-8 per formula unit (out of a total of  $N_{Zn}$ ), and  $N_{Hmim} / N_{H_2O}$  are the number of excess surface adsorbed Hmim / water molecules over the bulk stoichiometric ratio.  $\Delta \mu_{Hmim}$  and  $\Delta \mu_{H_2O}$  represent the relative chemical potentials,  $\Delta \mu_X = \mu_X - \mu_X^{\ominus}$  (X=Hmim, H<sub>2</sub>O), and  $\mu_X^{\ominus}$  is the chemical potential at standard conditions (298K, 1atm). Note that a similar procedure was utilized by Amirjalayer et al. to calculate the relative stability of several terminations of the MOF HKUST-1 on the basis of DFT.<sup>42</sup>

All slab terminations were constructed symmetrically between the two interfaces to balance surface dipoles, using a 15 Å vacuum gap to further minimize their periodic interactions. The Vienna Atomistic Simulation Package (VASP)<sup>43–46</sup> was utilized to conduct periodic DFT calculations of these surface slabs. These calculations utilized a projector-augmented wave (PAW)<sup>47,48</sup> treatment of core electrons in conjunction with a 600 eV energy cutoff. All structural optimizations utilized the PBE generalized gradient approximation exchange-correlation functional<sup>49</sup> with the atom positions of first two layers of the surface relaxed with fixed slab volume. Due to the large unit cell, the Brillouin zone was sampled only at the  $\Gamma$  point. Dispersion corrections were added via an empirical Grimme D3 correction.<sup>50</sup> In these optimization calculations, the energy was converged to 10<sup>-6</sup> eV and forces were converged to a tolerance of 0.01 eV/Å.

At the finite temperature, the Gibbs free energy of surface slab was computed by adding zero-point and entropy contributions to the DFT total energy,  $G_{slab}(T) = E_{slab} + \Delta ZPE - TS_{slab}$ . The  $pV$  term is neglected here because it makes only a trivial contribution to the

surface free energy.<sup>51</sup> Zero-point and entropy contributions were calculated using harmonic frequency analysis on the top layer of the surface (dashed red rectangle in Fig. 2). Similar approaches were used to compute the chemical potential of the molecular adsorbates (H<sub>2</sub>O and Hmim), with the addition of rotational and translational contributions; details can be found in the SI.

## Surface Phase Diagrams in Solution

Building on the above gas-phase surface phase diagrams, we also generate solution-phase diagrams by accounting for the differences in the associated experimental conditions as well as solvation effects. Note that, for simplicity, we consider only charge-neutral surface terminations (i.e. we do not consider charged surface terminations, which must be balanced by a diffuse double layer of ions from solution).

Since construction of a phase diagram requires only *relative* (and not absolute) surface free energies, we take as a reference a gas-phase ZIF termination with two excess adsorbed water molecules and two mim (“surf<sub>2/2</sub>”, see Fig. 2c). In the gas-phase, the surface energy of other terminations, relative to surf<sub>2/2</sub>, is given by

$$\Delta\gamma(g) = \frac{1}{2A} [G_{Slab}^{vac} - G_{surf_{2/2}}^{vac} - N_{Hmim}\mu_{Hmim}(g) - (N_{H_2O} - 4)\mu_{H_2O}(g)] \quad (3)$$

Note that there are two water molecules adsorbed on each side of the surf<sub>2/2</sub> termination and thus the total number of excess water molecules is 4 (see the last term in Eq. (3)).

Next we add a solvation correction to Eq. (3) to obtain the corresponding solution-phase

relative surface free energy,

$$\begin{aligned}
\Delta\gamma(aq) &= \frac{1}{2A} [G_{Slab}^{vac} + \Delta G_{slab}^{sol} - (G_{surf_{2/2}}^{vac} + \Delta G_{surf_{2/2}}^{sol}) \\
&\quad - N_{Hmim} \mu_{Hmim}(aq) - (N_{H_2O} - 4) \mu_{H_2O}(l)] \\
&= \frac{1}{2A} [\Delta G_{surf_{2/2}}^{vac} + \Delta\Delta G_{surf_{2/2}}^{sol} - N_{Hmim} \mu_{Hmim}(aq) - (N_{H_2O} - 4) \mu_{H_2O}(l)]
\end{aligned} \tag{4}$$

Here  $\Delta G_{surf_{2/2}}^{vac} = G_{Slab}^{vac} - G_{surf_{2/2}}^{vac}$  is the relative (gas-phase) free energy of the terminations, and  $\Delta\Delta G_{surf_{2/2}}^{sol} = \Delta G_{slab}^{sol} - \Delta G_{surf_{2/2}}^{sol}$  is the corresponding relative solvation correction.

Because water is the majority species in dilute aqueous solutions, we approximate the water chemical potential as a constant for a given temperature,  $\mu_{H_2O}(l) \approx \mu_{H_2O}^{\ominus}(c = 55M)$ , yielding our working expression,

$$\begin{aligned}
\Delta\gamma(c) &= \frac{1}{2A} [\Delta G_{surf_{2/2}}^{vac} + \Delta\Delta G_{surf_{2/2}}^{sol} - N_{Hmim} \mu_{Hmim}^{\ominus}(c = 1M) \\
&\quad - (N_{H_2O} - 4) \mu_{H_2O}^{\ominus}(c = 55M) - N_{Hmim} \Delta\mu_{Hmim}(c)]
\end{aligned} \tag{5}$$

where  $\Delta\mu_{Hmim}(c) = \mu_{Hmim}(c) - \mu_{Hmim}^{\ominus}(c = 1M)$ , and  $\mu_{Hmim}^{\ominus}(c = 1M)$  represents the standard chemical potential of Hmim in aqueous solution.

## Evaluation of Solvation Corrections

Utilization of Eq. (5) requires the evaluation of several quantities:  $\Delta G_{surf_{2/2}}^{vac}$ ,  $\mu_{Hmim}^{\ominus}(c = 1M)$ ,  $\mu_{H_2O}^{\ominus}(c = 55M)$  and  $\Delta\Delta G_{surf_{2/2}}^{sol}$ ;  $\Delta G_{surf_{2/2}}^{vac}$  can be easily obtained from gas phase calculation, as described in the prior section. We compute  $\mu_{Hmim}^{\ominus}(c = 1M)$  via correction from the corresponding gas-phase chemical potential,  $\mu_{Hmim}^{\ominus}(p = 1atm)$ ,

$$\mu_{Hmim}^{\ominus}(c = 1M) = \mu_{Hmim}^{\ominus}(p = 1atm) + \Delta G_{sol(Hmim)}^{\ominus} \tag{6}$$

The standard solvation free energy,  $\Delta G_{sol(Hmim)}^\ominus$ , was evaluated by adding the solvation free energy obtained via the experimentally-measured air-water partitioning coefficient of imidazole (Him)<sup>52</sup> to the simulated solvation free energy difference between Hmim and Him. The simulated Gibbs free energy change of solvation was computed via thermodynamic integration (TI), by gradually tuning the adsorbate-solvent interaction using a coupling parameter,  $\lambda$ , which slowly decouples the solute and solvent interaction. The free energy difference between these two states was computed as:

$$\Delta G_{0 \rightarrow 1} = \int_0^1 \left\langle \frac{\partial U(\lambda)}{\partial \lambda} \right\rangle_\lambda d\lambda \quad (7)$$

Complete details can be found in the SI.

We compute  $\mu_{\text{H}_2\text{O}}^\ominus(c = 55M)$  via equilibrium with the experimentally-measured vapor pressure,

$$\begin{aligned} \mu_{\text{H}_2\text{O}}^\ominus(c = 55M) &= \mu_{\text{H}_2\text{O}}^\ominus(p = 1atm) - \Delta G_{vap(\text{H}_2\text{O})}^\ominus \\ &= \mu_{\text{H}_2\text{O}}^\ominus(p = 1atm) + RT \ln \frac{p_{vap}}{p^\ominus} \end{aligned} \quad (8)$$

where  $p_{vap}$  is measured liquid water vapor pressure at 298K (0.031 atm).<sup>53</sup>

To evaluate the relative solvation free energy of various terminated ZIF-8 surfaces, we utilized TI coupled with the so-called dual topology approach, involving the alchemical transformation / thermodynamic cycle demonstrated in Fig. 1. Using a pair of such alchemical mutations, one *in vacuo* and the other in solution, we obtained the required solvation correction as  $\Delta \Delta G^{sol} = \Delta G_{sol}^2 - \Delta G_{sol}^1 = \Delta G_{alch}^2 - \Delta G_{alch}^1$ .

For these alchemical TI calculations, we utilized an initial simulation box that was constructed with a  $(2 \times 2 \times 1)$  ZIF-8 (110) surface slab solvated with 1420 water molecules generated using the Packmol<sup>54</sup> package. The ZIF-FF<sup>55</sup> and TIP4P-Ew<sup>56</sup> force fields were applied to describe ZIF surface and water, respectively. The cut off radius for van der Waals

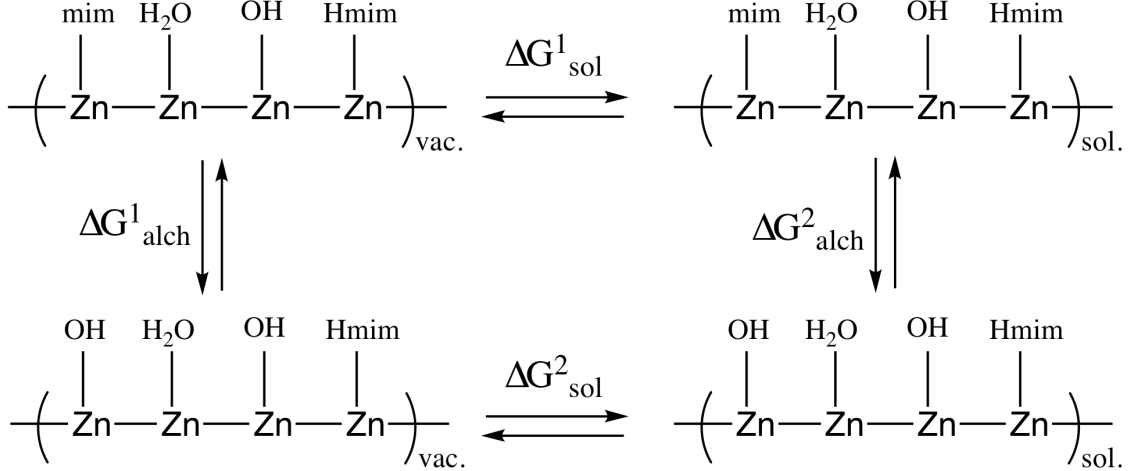


Figure 1: Thermodynamic cycle used in alchemical transformation of surface termination "surf<sub>2/2</sub>" to "surf<sub>1/3</sub>".

and Coulomb interactions were set to 13 Å and 10 Å. Point charges were assigned to each atom using the DDEC<sup>57,58</sup> method. Electrostatic and van der Waals interactions were decoupled using separate  $\lambda_{elec}$  and  $\lambda_{vdw}$  parameters, using 10 equally spaced points for each region; several additional points were added for  $\lambda_{vdw}$  in regions of rapid change. Van der Waals interactions were scaled using a soft-core potential to avoid singularities. NPT simulations were run using the LAMMPS<sup>59</sup> simulation package. We utilized 5 ns for equilibration and a subsequent 10 ns production run for each  $\lambda$ . The temperature was fixed at 300 K using Nose-Hoover thermostat and a 1 fs timestep. The pressure was controlled via a Nose-Hoover barostat (damping time of 1000 fs). The particle-particle particle-mesh (PPPM)<sup>60</sup> method was used to calculate the electrostatic interaction.

## Surface Phase Diagrams in DMF Solvent

Surface phase diagrams in DMF solvent were calculated analogously to the aqueous case. Beginning with the corresponding gas-phase results, we computed solvation corrections via TI. We treat  $\mu_{DMF}$  (the solvent chemical potential) as a constant evaluated for the pure liquid. For the TI simulations, the initial simulation box was constructed with a  $(2 \times 2 \times 1)$

ZIF-8 (110) surface slab and 330 DMF molecules, using the OPLS-AA force field for DMF.<sup>61</sup>

## Results and Discussion

### Surface Structures

We list all possible surface terminations in Table 1 and organize them in three categories: those enriched in the Hmim linker (L), over the stoichiometric ratio; those with a stoichiometric amount of Hmim, but potentially additional adsorbed solvent ( $\text{ZnL}_2$ ); and those deficient in Hmim as compared to the stoichiometric ration (Zn-rich). Since our surface slab is symmetrically terminated on both sides, we denote the surface terminations based on the number of adsorbed Hmim(mim)/ $\text{H}_2\text{O}$ (OH) on a single side. For example, we refer to the bare/stoichiometric surface configuration with two dangling imidazolate linkers (and no adsorbed solvent) as “surf<sub>2/0</sub>”. Here the 2 denotes two imidazole-like groups (Hmim or mim), and 0 indicates no water-like groups ( $\text{H}_2\text{O}$  or OH) present on the surface termination; this stoichiometric termination is shown in Fig. 2a, alongside four additional possible terminations. For each termination type, the corresponding VASP-optimized configuration and energy are shown in the SI.

Starting with the bare stoichiometric surface, surf<sub>2/0</sub>, we consider the adsorption of additional adsorbates ( $\text{H}_2\text{O}$  or Hmim). We find that adsorption of additional Hmim is quite favorable, with a binding energy of 1.98 eV; this large binding energy originates both from direct coordination of the Zn and N and hydrogen bonding between adjacent Hmim and mim linkers, as shown in Fig. 3a. In the case of water adsorption, we find that dissociative adsorption of a single water (1.59 eV) is more stable as compared to associative chemisorption (0.72 eV). As shown in Fig. 3b, the dissociative configuration yields not only a stable hydrogen bond between adjacent Hmim and mim, but also a stronger Zn-O bond compared to Zn- $\text{H}_2\text{O}$  chemisorption.

Table 1: Summary of Surface Terminations of ZIF-8(110)

Category	Termination	Number of Configurations <sup>a</sup>	$N_{\text{Hmim}}$	$N_{\text{H}_2\text{O}}$
L-rich	surf <sub>4/0</sub>	3	4	0
	surf <sub>3/0</sub>	3	2	0
	surf <sub>3/1</sub>	6	2	2
ZnL <sub>2</sub>	surf <sub>2/0</sub>	3	0	0
	surf <sub>2/1</sub>	9	0	2
	surf <sub>2/2</sub>	12	0	4
Zn-rich	surf <sub>1/1</sub>	3	-2	2
	surf <sub>1/2</sub>	9	-2	4
	surf <sub>1/3</sub>	6	-2	6
	surf <sub>0/2</sub>	3	-4	4
	surf <sub>0/3</sub>	3	-4	6
	surf <sub>0/4</sub>	3	-4	8

a. The number of configurations listed here shows the possible combinations of relative linker positions. DFT energies of the most stable configurations for each termination are shown in SI.

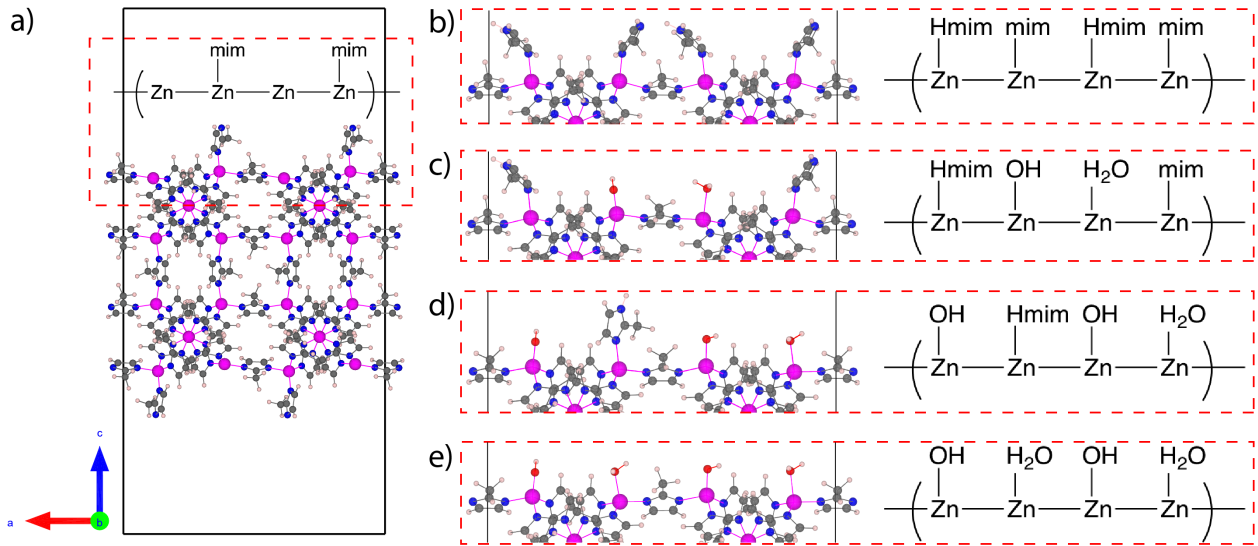


Figure 2: Structure of ZIF-8 (110) surface with (a) stoichiometric termination surf<sub>2/0</sub> (left); examples of (b) surf<sub>4/0</sub>, (c) surf<sub>2/2</sub>, (d) surf<sub>1/3</sub>, (e) surf<sub>0/4</sub> (right), alongside a schematic depiction

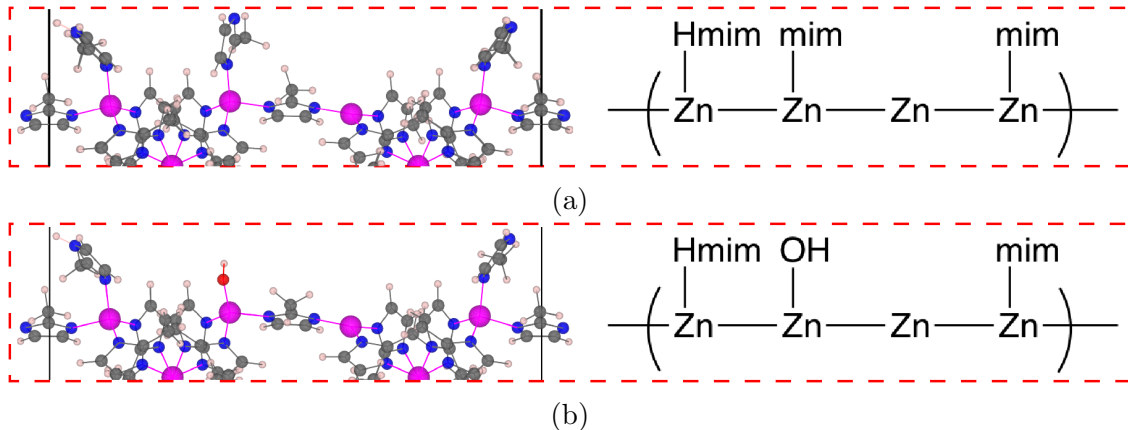


Figure 3: ZIF-8 (110) surface termination with (a) one Hmim adsorbed (i.e.  $\text{surf}_{3/0}$ ); (b) one water dissociated adsorption (i.e.  $\text{surf}_{2/1}$ )

## Surface Phase Diagram in Gas Phase

Based on the above DFT-calculated energies / free energies of the various ZIF surface terminations, we utilize Eq. (2) to calculate the corresponding surface energies as a function of  $\Delta\mu_{\text{Hmim}}$  and  $\Delta\mu_{\text{H}_2\text{O}}$  at room temperature (298K), typical of post-synthetic conditions (humid air) under which ZIFs might be utilized, and also representative of those used during ex situ ZIF characterization studies. These surface energies were used to construct a two-dimensional surface phase diagram, where the Hmim and  $\text{H}_2\text{O}$  concentrations are given as either partial pressures or relative chemical potentials; see Fig. 4.

We find that the  $\text{surf}_{4/0}$  termination (red region) is the dominant surface structure except at extremely low partial pressures of Hmim. Such low partial pressures (lower than  $10^{-10}$  bar) are not unreasonable under post-synthetic conditions, where the only free Hmim likely originates from desorption from the surface. At sufficiently low partial pressure of Hmim, water becomes the dominant surface species. Under such conditions, when the partial pressure of water is larger than  $10^{-3}$  bar, the surface is fully covered by water and surface imidazolate linkers are replaced by hydroxyl groups, yielding the  $\text{surf}_{0/4}$  termination; this transition is explored in more detail below, *vide infra*. As the partial pressure of water drops,

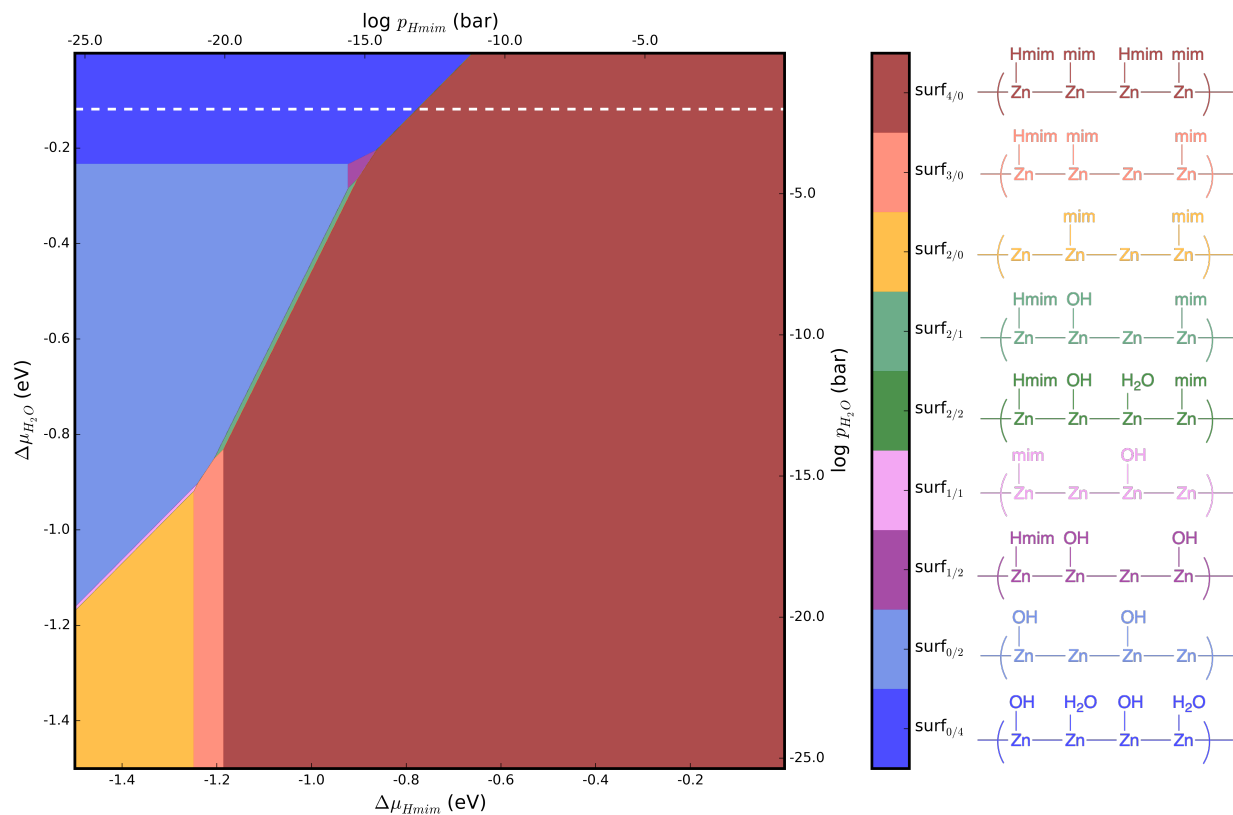


Figure 4: ZIF-8 surface phase diagram at 298K in gaseous atmosphere

this replacement is incomplete, and may even expose undercoordinated Zn sites. When the partial pressure of water is extremely low (lower than  $10^{-20}$  bar), the stoichiometric (undercoordinated)  $\text{surf}_{2/0}$  termination becomes the most stable phase (yellow region), due to the low partial pressure of all available adsorbates.

Focusing specifically on the case of a ZIF surface under humid air (50% relative humidity,  $\sim 0.016$  atm  $\text{H}_2\text{O}$ <sup>62</sup>), we examine the corresponding cross-section of the two-dimensional phase diagram (white dashed lined). The resulting one-dimensional surface phase diagram is shown as a function of partial pressure of Hmim in Fig. 5. We show only those terminations corresponding to full surface coverage, since all partial coverages are unstable under these conditions (see SI for details). We find that the surface termination evolves from  $\text{surf}_{4/0}$  to  $\text{surf}_{0/4}$  at a (very low) Hmim partial pressure of about  $10^{-15}$  bar. Under such conditions, and given 50% relative humidity, the water concentration is sufficiently high that the replacement of surface Hmim/mim species by  $\text{H}_2\text{O}/\text{OH}$  is complete.

A practical challenge in applying this phase diagram is to identify a “reasonable” Hmim partial pressure, which in turn determines the equilibrium surface termination. We utilize the following argument to make a qualitative estimate: Given a typical ZIF-8 crystal size of  $1 \mu\text{m}$ , the *external* surface area (assuming spherical crystals) is approximately  $10 \text{ m}^2/\text{g}$ ;<sup>63</sup> we postulate that only those adsorbates present on the external crystallite surface are prone to loss/desorption. Assuming a  $1\text{g}$  sample enclosed in a  $1 \text{ m}^3$  container and equilibrated at room temperature, the desorption of even  $\sim 1\%$  of the surface Hmim from the initial surface would yield a Hmim partial pressure of  $10^{-10}$  atm. Even under this low partial pressure, Fig. 4 demonstrates that the equilibrium surface remains fully covered with imidazole (Hmim or mim) species,  $\text{surf}_{4/0}$ . These conclusions are essentially independent of the water partial pressure, until extremely low Hmim partial pressures (such as might be achieved by prolonged drying under vacuum). These results are also consistent with high resolution transmission electron microscopy (HRTEM) experiments by Zhu et al. on the ZIF-8 (110) surface.<sup>25</sup>

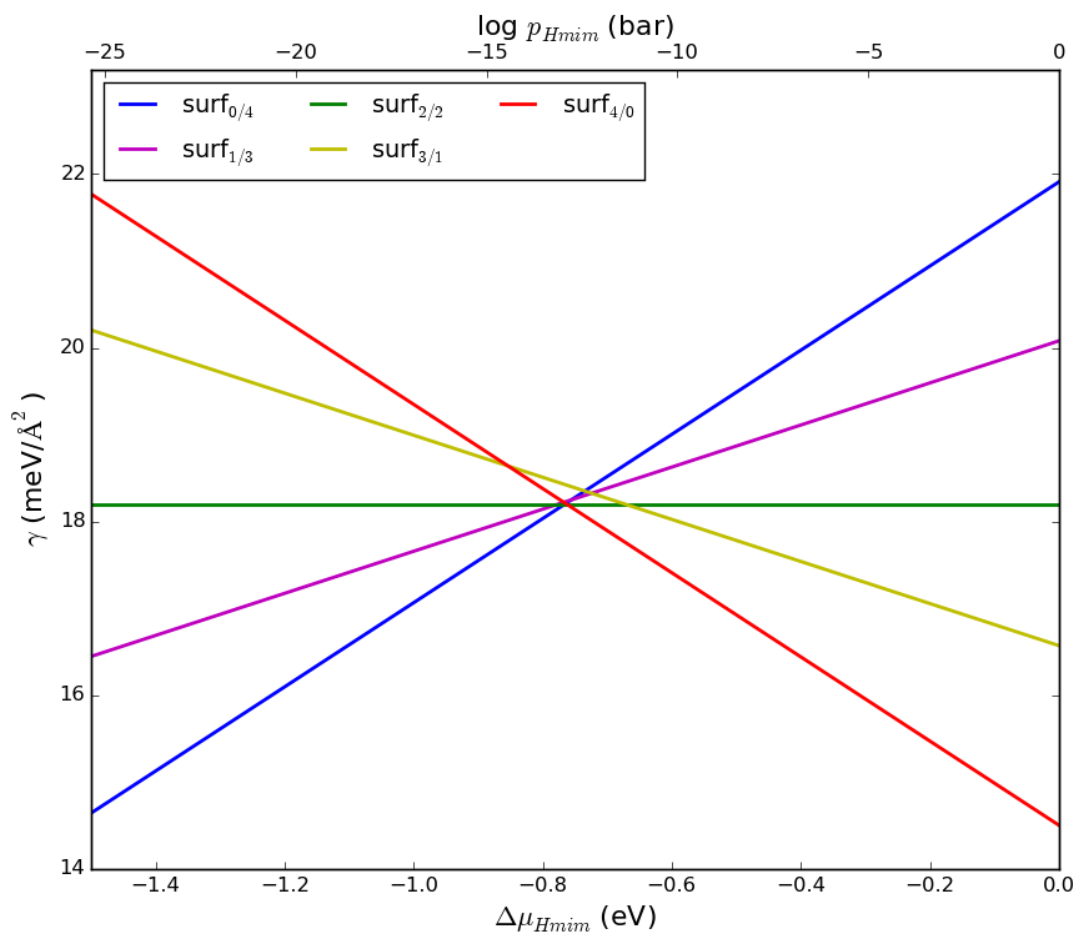


Figure 5: ZIF-8 surface phase diagram at 298K in gas phase at 50% relative humidity (only full coverage terminations shown)

In their work, ZIF-8 crystals were synthesized in aqueous solution at room temperature with a large Hmim excess.<sup>25</sup> However, the HRTEM images were taken post-synthesis after the crystals were washed and dried for an extended period at 363 K, which should allow for quasi-equilibration of the surface, as outlined above. Their HRTEM results showed an ‘armchair’-type termination, with surface  $\text{Zn}^{2+}$  ions capped by Hmim, and consistent with the prediction the surface phase diagram.

## Surface Phase Diagram in Aqueous Solution

Given the growing prevalence of room temperature (vs. solvothermal) synthesis methods for ZIFs, which often employ aqueous (vs. organic) solvents, we further examine the surface phase diagram in aqueous solution at room temperature. As mentioned previous, we consider only the charge-neutral surface terminations and limit our discussion to those with full coverage:  $\text{surf}_{4/0}$ ,  $\text{surf}_{3/1}$ ,  $\text{surf}_{2/2}$ ,  $\text{surf}_{1/3}$ ,  $\text{surf}_{0/4}$ . These solution-phase surface phase diagrams can be obtained from the prior gas-phase diagrams by accounting for solvation effects, as in Eq. (5). We report our results both in terms of excess Hmim chemical potential and concentrations, using  $\Delta\mu_{hmim} = -kT \ln c_{\text{Hmim}}/c^\ominus$ , where  $c^\ominus = 1 \text{ M}$ ; the resulting phase diagram is shown in Fig. 6.

In contrast to the gas-phase, post-synthetic scenario, quantifying an appropriate Hmim concentration is more straightforward under synthetic conditions. Note, however, that two distinct regimes are relevant, depending on whether excess or stoichiometric Hmim were utilized during the synthesis. In the former case, significant ( $\sim$ molar) concentrations of Hmim remain in solution after crystallization. In the latter case, in contrast, it is likely that only very low Hmim concentrations will persist, governed by the extremely largely complexation constant for imidazole species by Zn ( $10^{13.4}$ ).<sup>64</sup> Note that in both cases, the appropriate Hmim concentration,  $c_{\text{Hmim}}$ , should be properly interpreted as the *excess* (free) solution-phase Hmim upon completion of the crystallization.

As shown in Fig. 6, when the excess Hmim concentration is greater than  $\sim 10\text{mM}$ , the equilibrium surface is entirely imidazole covered,  $\text{surf}_{4/0}$ . However, as the excess Hmim concentration further decreases, solvent progressively incorporates on the surface, transforming from  $\text{surf}_{4/0}$  to  $\text{surf}_{1/3}$ . When the excess Hmim concentration drops to substantially lower values ( $\sim 10^{-5}\text{ M}$ ), the ZIF-8 (110) surface becomes entirely terminated with hydroxyl groups and water molecules,  $\text{surf}_{0/4}$ . Comparing this 1D surface phase diagram with the corresponding gas-phase results, we see qualitatively similar trends (i.e. the expected transition from Hmim- to water-covered, with changing Hmim concentration) but substantial differences in the transition regimes. In particular, this gas-phase transition region occurs only for extraordinarily small Hmim partial pressures, which are unlikely to be realized in most situations. In contrast, the solution-phase transition concentration should be easily achievable, depending on the synthetic details.

To make a more direct connection with experimental results, we can also account for the role of solution pH. In particular, the excess  $c_{\text{Hmim}}$  varies with solution pH according to the speciation of imidazole. Since the pKa of Hmim is 15.1, we focus on the regime where  $\text{pH} < \text{pKa}$  and the dominant solution-phase imidazole species are Hmim and protonated  $\text{H}_2\text{mim}^+$  (excluding the minority  $\text{mim}^-$ ). Note that of these majority species, only Hmim can coordinate with the surface (since  $\text{H}_2\text{mim}^+$  contains no free N groups); this also ensures that the dominant surface terminations will remain charge neutral. We utilize the known equilibrium constants for Hmim to calculate its speciation with pH (and  $c_{\text{Hmim}}$ , in particular); see the SI. We then use these results to construct a surface phase diagram at a fixed *total* Hmim concentration (all imidazole species) of 1M at various pH values; see Fig. 7.

We find that the resulting equilibrium surface termination exhibits a strong pH dependence, which can be divided into three regimes. For  $\text{pH} > 5.7$ , the imidazole speciation is dominated by Hmim. In this case, the excess concentration of Hmim is sufficiently high that the ZIF surface is imidazole covered ( $\text{surf}_{4/0}$ ). However, as the pH decreases, protonation of

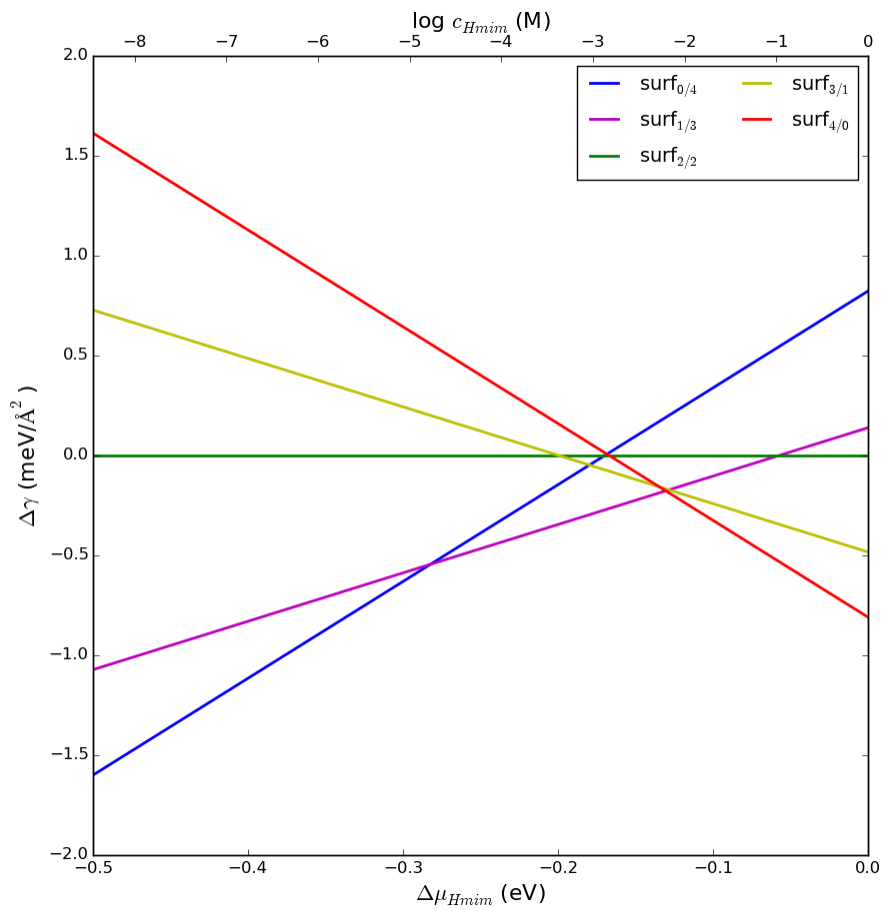


Figure 6: ZIF-8 surface phase diagram at 298K in aqueous solution

the Hmim becomes increasingly important, lowering the free Hmim concentration. In this regime, we see partial replacement of Hmim by solvent species, reflecting  $\text{surf}_{1/3}$  termination (marked as purple) in the plot. At even lower pH ( $\sim < 3$ ), the  $\text{H}_2\text{mim}^+$  species dominate and the solvent termination is essentially complete, with the surface dominated by water and -OH groups.

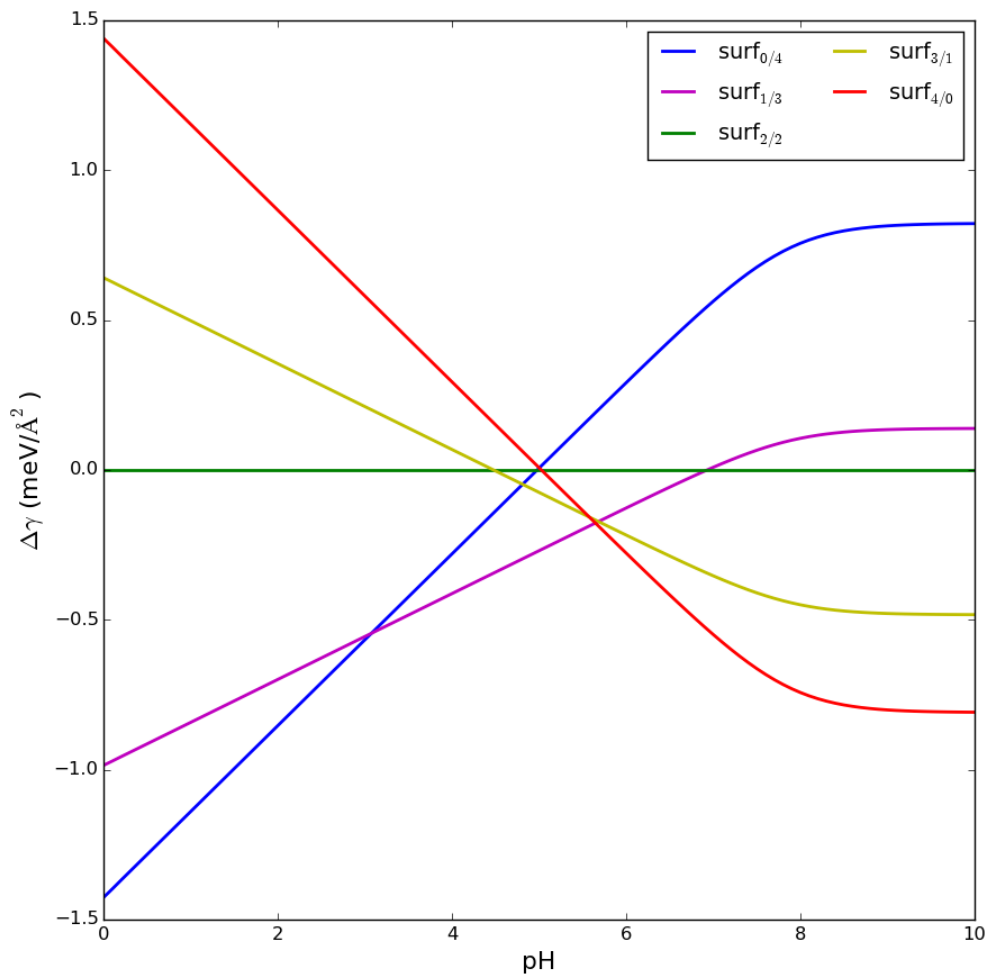


Figure 7: ZIF-8 surface phase diagram at 298K as a function of pH in aqueous solution

The above discussion and pH-dependent surface phase diagram clearly predict a wa-

ter/hydroxyl terminated ZIF surface at low pH ( $\sim < 5.7$ ). These conclusions are consistent with direct experimental evidence obtained via both X-ray photoelectron spectroscopy (XPS) and Fourier transform infrared spectroscopy (FTIR) characterization of ZIF-8 {110} facets under mildly acidic conditions.<sup>27</sup> Pang et al. synthesized ZIF-8 rhombic dodecahedra crystallites at room temperature in water and subsequently exposed them to an aqueous  $\text{SO}_2$  solution. They observed a decrease of N 1s peak intensity and the increase of O 1s peak intensity in XPS spectra, suggesting that surface imidazoles were replaced by hydroxyls during a degradation process under mildly acidic conditions. This observation was accompanied by an increase in the IR adsorption intensity in the OH stretching region ( $3400\text{-}3500\text{ cm}^{-1}$ ) in the FTIR spectra, further supporting the  $\text{Zn}(\text{OH})_2$  termination. In addition, they authors also observed more obvious degradation with increasing  $\text{SO}_2$  concentration via SEM. Similar phenomena were found by Avcı et al. upon the exposure of ZIF-8 crystal samples to HCl solutions.<sup>65</sup> In both cases, these results are consistent with the predictions from the pH-dependent ZIF surface phase diagram.

## Surface Phase Diagram in DMF Solution

Using similar approach, we replace the water solvent with DMF; an important difference in this case arises due to the aprotic nature of DMF, ruling out terminations involving dissociative adsorption. We consider the following full-coverage surface terminations:  $\text{surf}_{4/0}$ ,  $\text{surf}_{3/1}$ , and  $\text{surf}_{2/2}$ , where the second index now refers to the number of adsorbed DMF molecules. In addition, since DMF is often used in solvothermal ZIF synthesis, we compute the surface free energies at a higher temperature of 373K; the resulting surface phase diagram is shown in Fig. 8.

Just as in the case of room-temperature aqueous solution (Fig. 6), we find that the surface phase diagram in DMF predicts an imidazole-terminated  $\text{surf}_{4/0}$  surface outside of low Hmim concentrations. As the Hmim concentration decreases below the  $\sim 10\mu\text{M}$  regime, DMF

incorporation begins ( $\text{surf}_{3/1}$ ) and this process continues as the free Hmim concentration drops below  $\sim 1\mu\text{M}$  ( $\text{surf}_{2/2}$ ). Note that the transition from a fully-imidazole to a partially-solvent-covered termination occurs at substantially lower Hmim concentrations as compared to the aqueous case. This difference arises because the gas-phase binding energy of a single DMF molecule (1.30 eV) is smaller than the dissociative binding energy of a single water (1.59 eV); in turn, both solvent species display a smaller binding energy as compared to Hmim (1.98 eV). Given that the solvation free energy differences between water and DMF are modest compared to these binding energy differences, it is primarily the relative solvent binding energies that govern the differences in the phase diagrams.

In connecting to prior experimental observations under DMF, it is important to note that most solvothermal ZIF syntheses utilize a stoichiometric ratio of Zn to Hmim (1:2), in contrast to room temperature aqueous syntheses that often employ a large excess of Hmim. In other words, upon completion of the reaction, we would expect only very small residual concentrations of free Hmim. A rough order-of-magnitude estimate for the residual Hmim can be obtained by using the solubility constant for ZIFs ( $10^{13.4}$ ),<sup>64</sup> which would predict a saturated concentration of imidazole species of  $\sim 10^{-5}\text{M}$ . In this regime, the surface phase diagram predicts partial DMF surface incorporation, i.e.  $\text{surf}_{3/1}$ . This result is consistent with the prior experimental observations by Attfield and coworkers.<sup>23</sup> In their work, ZIF-8 substrate crystals were initially prepared using a stoichiometric ratio of Zn:Hmim under solvothermal conditions (373 K) in DMF. In situ AFM was then used to monitor the growth of the crystalline {110} facets in a diluted methanol/DMF solution. Via step heights analysis, those authors demonstrated that the ZIF-8 crystal surface plane were not terminated with pure secondary building units (i.e.  $[\text{Zn}(\text{mim})_4]^{2-}$ ), but rather involved surface  $\text{Zn}^{2+}$  ions coordinated to 3 linkers (from the underlying bulk ZIF) and one solvent. This conclusion, based upon AFM analysis, is consistent with our predicted solvent-terminated surface under such conditions.

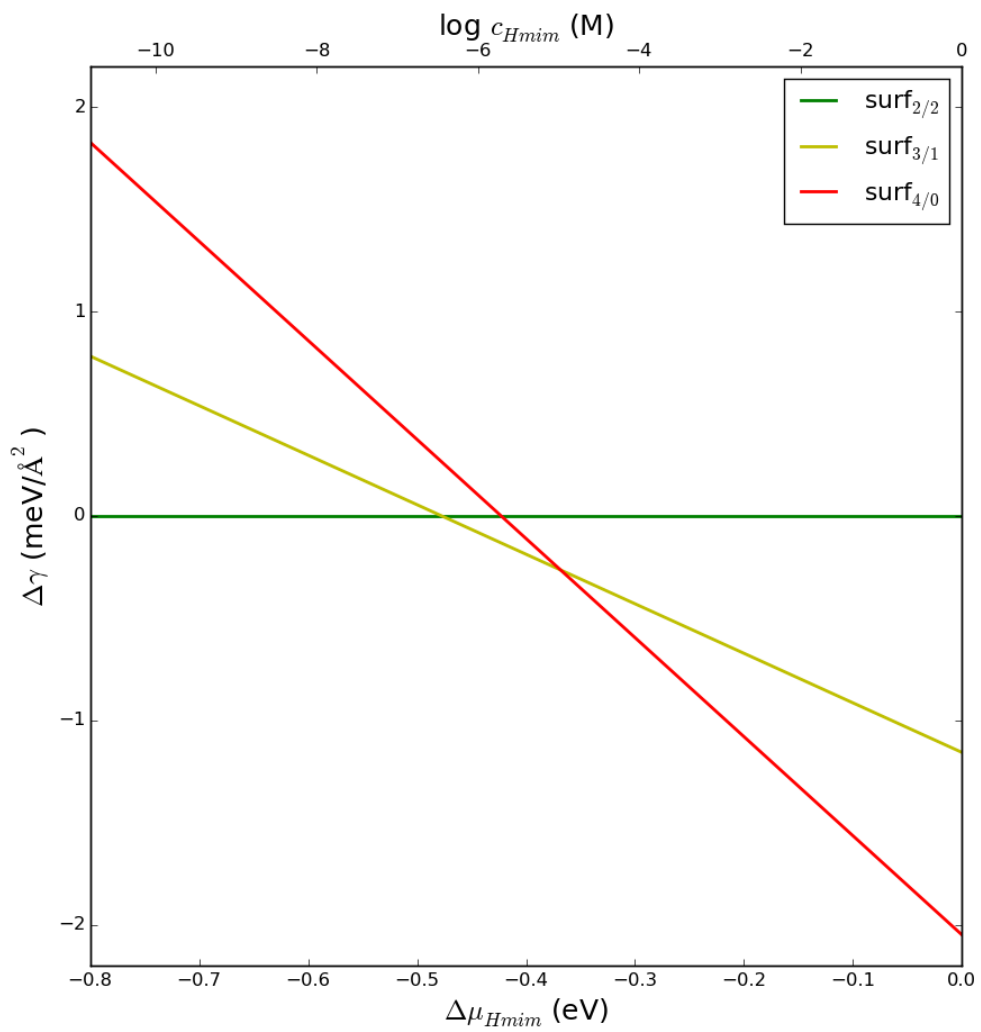


Figure 8: ZIF-8 surface phase diagram at 373K in DMF solution

# Conclusions

Using a combination of DFT-calculated energetics and MD-calculated solvation effects, we have constructed surface phase diagrams for ZIF materials that are valid over a wide range of conditions. In the case of gas-phase “post-synthetic” conditions, we find that ZIF surfaces are almost inevitably terminated primarily by imidazole-related species (“surf<sub>4/0</sub>”), rather than solvent. This termination remains stable even under high relative humidity and extremely low Hmim partial pressure, and thus we expect that it would be altered only via prolonged heating under vacuum (to remove any desorbed Hmim).

In the case of solution, the situation is more complex. Under high solute-phase imidazole concentrations, a fully imidazole terminated surf<sub>4/0</sub> surface remains quite stable. However, at low pH, where the free (unprotonated) Hmim concentrations becomes low, partial (surf<sub>2/2</sub>) and even total (surf<sub>0/4</sub>) solvent incorporation may occur. These predictions are consistent with prior experimental observations of ZIF evolution under acid exposure, which was shown to result in water/hydroxyl incorporation as detected via both IR and XPS.<sup>27</sup> Small free Hmim concentrations can also arise from the use of stoichiometric Zn:Hmim ratios, e.g. as is common in solvothermal synthesis – cases where in situ AFM has also shown evidence for surface solvent incorporation, consistent with our phase diagram predictions.<sup>23</sup>

Although kinetic factors (beyond thermodynamics) can also play an important role in the observed ZIF surface termination, these phase diagrams nonetheless outline the crucial driving forces that ultimately govern the stability of various ZIF terminations. We anticipate that these diagrams may provide a useful predictive tool in understanding how ZIF surface structure may be altered / controlled as a function of both synthetic and post-synthetic conditions, with associated impacts on ZIF interfacial properties, including those governing surface mass transport barriers.

## Acknowledgement

This work was supported by Chemical Sciences, Geosciences and Biosciences Division, Office of Basic Energy Sciences, Office of Science, U.S. Department of Energy, under award DE-SC0014059. Computational resources were provided by the UW- Madison Center for High Throughput Computing (CHTC) in the Department of Computer Sciences. The CHTC is supported by UW-Madison, the Advanced Computing Initiative, the Wisconsin Alumni Research Foundation, the Wisconsin Institutes for Discovery, and the National Science Foundation, and is an active member of the Open Science Grid, which is supported by the National Science Foundation and the U.S. Department of Energy's Office of Science. J.R.S is a Camille Dreyfus Teacher-Scholar.

## Supporting Information Available

Optimized configurations of ZIF-8 (110) surfaces; details of Gibbs free energy calculation; table of DFT energies / Gibbs free energies; details of solvation free energy calculations; figure of ZIF-8 surface phase diagram at 298K and 50 percent RH; Hmim speciation with pH.

## References

- (1) Stock, N.; Biswas, S. Synthesis of Metal-Organic Frameworks (MOFs): Routes to Various MOF Topologies, Morphologies, and Composites. *Chem. Rev.* **2012**, *112*, 933–969.
- (2) Furukawa, H.; Cordova, K. E.; O’Keeffe, M.; Yaghi, O. M. The Chemistry and Applications of Metal-Organic Frameworks. *Science* **2013**, *341*.
- (3) Van Vleet, M. J.; Weng, T.; Li, X.; Schmidt, J. R. In Situ, Time-Resolved, and Mechanistic Studies of Metal-Organic Framework Nucleation and Growth. *Chem. Rev.* **2018**, *118*, 3681–3721.
- (4) Murray, L. J.; Dincă, M.; Long, J. R. Hydrogen Storage in Metal–Organic Frameworks. *Chem. Soc. Rev.* **2009**, *38*, 1294–1314.
- (5) Chaemchuen, S.; Kabir, N. A.; Zhou, K.; Verpoort, F. Metal–Organic Frameworks for Upgrading Biogas via CO<sub>2</sub> Adsorption to Biogas Green Energy. *Chem. Soc. Rev.* **2013**, *42*, 9304–9332.
- (6) Tanh Jeazet, H. B.; Staudt, C.; Janiak, C. Metal–Organic Frameworks in Mixed-Matrix Membranes for Gas Separation. *Dalton Trans.* **2012**, *41*, 14003–14027.
- (7) Qiu, S.; Xue, M.; Zhu, G. Metal–Organic Framework Membranes: From Synthesis to Separation Application. *Chem. Soc. Rev.* **2014**, *43*, 6116–6140.
- (8) Liu, J.; Chen, L.; Cui, H.; Zhang, J.; Zhang, L.; Su, C.-Y. Applications of Metal–Organic Frameworks in Heterogeneous Supramolecular Catalysis. *Chem. Soc. Rev.* **2014**, *43*, 6011–6061.
- (9) Farrusseng, D.; Aguado, S.; Pinel, C. Metal–Organic Frameworks: Opportunities for Catalysis. *Angew. Chem. Int. Ed.* **2009**, *48*, 7502–7513.
- (10) Kreno, L. E.; Leong, K.; Farha, O. K.; Allendorf, M.; Van Duyne, R. P.; Hupp, J. T. Metal–Organic Framework Materials as Chemical Sensors. *Chem. Rev.* **2012**, *112*, 1105–1125.
- (11) Rojas, S.; Wheatley, P. S.; Quartapelle-Procopio, E.; Gil, B.; Marszalek, B.; Morris, R. E.; Barea, E. Metal–Organic Frameworks as Potential Multi-Carriers of Drugs. *CrystEngComm* **2013**, *15*, 9364–9367.
- (12) Horcajada, P.; Gref, R.; Baati, T.; Allan, P. K.; Maurin, G.; Couvreur, P.; Férey, G.; Morris, R. E.; Serre, C. Metal–Organic Frameworks in Biomedicine. *Chem. Rev.* **2012**, *112*, 1232–1268.
- (13) Zhou, H.-C.; Long, J. R.; Yaghi, O. M. Introduction to Metal–Organic Frameworks. *Chem. Rev.* **2012**, *112*, 673–674.

- (14) Zacher, D.; Schmid, R.; Wöll, C.; Fischer, R. A. Surface Chemistry of Metal-Organic Frameworks at the Liquid-Solid Interface. *Angew. Chem. Int. Ed.* **2011**, *50*, 176–199.
- (15) Dutta, A.; Tymiąska, N.; Zhu, G.; Collins, J.; Lively, R. P.; Schmidt, J. R.; Vasenkov, S. Influence of Hydrogen Sulfide Exposure on the Transport and Structural Properties of the Metal–Organic Framework ZIF-8. *J. Phys. Chem. C* **2018**, *122*, 7278–7287.
- (16) Gao, M.; Li, H.; Yang, M.; Gao, S.; Wu, P.; Tian, P.; Xu, S.; Ye, M.; Liu, Z. Direct Quantification of Surface Barriers for Mass Transfer in Nanoporous Crystalline Materials. *Commun. Chem.* **2019**, *2*, 1–10.
- (17) Guo, Y.; Peng, X. Mass Transport through Metal Organic Framework Membranes. *Sci. China Mater.* **2019**, *62*, 25–42.
- (18) Heinke, L.; Wöll, C. Surface-Mounted Metal–Organic Frameworks: Crystalline and Porous Molecular Assemblies for Fundamental Insights and Advanced Applications. *Adv. Mater.* **2019**, *31*, 1806324.
- (19) Chen, L.; Duan, B.; Luo, Q.; Gu, Z.; Liu, J.; Duan, C. Facet-Dependent Catalytic Activity of ZIF-8 Nanocubes and Rhombic Dodecahedra Based on Tracing Substrate Diffusion in Pores by SERS: A Case Study for Surface Catalysis of MOFs. *Catal. Sci. Technol.* **2016**, *6*, 1616–1620.
- (20) Park, K. S.; Ni, Z.; Côté, A. P.; Choi, J. Y.; Huang, R.; Uribe-Romo, F. J.; Chae, H. K.; O’Keeffe, M.; Yaghi, O. M. Exceptional Chemical and Thermal Stability of Zeolitic Imidazolate Frameworks. *Proc. Natl. Acad. Sci. U.S.A.* **2006**, *103*, 10186–91.
- (21) Chen, B.; Yang, Z.; Zhu, Y.; Xia, Y. Zeolitic Imidazolate Framework Materials: Recent Progress in Synthesis and Applications. *J. Mater. Chem. A* **2014**, *2*, 16811–16831.
- (22) Pimentel, B. R.; Parulkar, A.; Zhou, E.-k.; Brunelli, N. A.; Lively, R. P. Zeolitic Imidazolate Frameworks: Next-Generation Materials for Energy-Efficient Gas Separations. *ChemSusChem* **2014**, *7*, 3202–3240.
- (23) Moh, P. Y.; Cubillas, P.; Anderson, M. W.; Attfield, M. P. Revelation of the Molecular Assembly of the Nanoporous Metal Organic Framework ZIF-8. *J. Am. Chem. Soc.* **2011**, *133*, 13304–13307.
- (24) Tian, F.; Cerro, A. M.; Mosier, A. M.; Wayment-Steele, H. K.; Shine, R. S.; Park, A.; Webster, E. R.; Johnson, L. E.; Johal, M. S.; Benz, L. Surface and Stability Characterization of a Nanoporous ZIF-8 Thin Film. *J. Phys. Chem. C* **2014**, *118*, 14449–14456.
- (25) Zhu, Y.; Ciston, J.; Zheng, B.; Miao, X.; Czarnik, C.; Pan, Y.; Sougrat, R.; Lai, Z.; Hsiung, C. E.; Yao, K. et al. Unravelling Surface and Interfacial Structures of a Metal–Organic Framework by Transmission Electron Microscopy. *Nat. Mater.* **2017**, *16*, 532–536.

- (26) Chizallet, C.; Lazare, S.; Bazer-Bachi, D.; Bonnier, F.; Lecocq, V.; Soyer, E.; Quoineaud, A.-A.; Bats, N. Catalysis of Transesterification by a Nonfunctionalized Metal-Organic Framework: Acido-Basicity at the External Surface of ZIF-8 Probed by FTIR and ab Initio Calculations. *J. Am. Chem. Soc.* **2010**, *132*, 12365–12377.
- (27) Pang, S. H.; Han, C.; Sholl, D. S.; Jones, C. W.; Lively, R. P. Facet-Specific Stability of ZIF-8 in the Presence of Acid Gases Dissolved in Aqueous Solutions. *Chem. Mater.* **2016**, *28*, 6960–6967.
- (28) Semino, R.; Ramsahye, N. A.; Ghoufi, A.; Maurin, G. Microscopic Model of the Metal–Organic Framework/Polymer Interface: A First Step toward Understanding the Compatibility in Mixed Matrix Membranes. *ACS Applied Materials & Interfaces* **2016**, *8*, 809–819.
- (29) Chizallet, C.; Bats, N. External Surface of Zeolite Imidazolate Frameworks Viewed Ab Initio: Multifunctionality at the Organic-Inorganic Interface. *J. Phys. Chem. Lett.* **2010**, *1*, 349–353.
- (30) Cravillon, J.; Munzer, S.; Lohmeier, S.-j.; Feldhoff, A.; Huber, K.; Wiebcke, M. Rapid Room-Temperature Synthesis and Characterization of Nanocrystals of a Prototypical Zeolitic Imidazolate Framework. *Chem. Mater.* **2009**, *21*, 1410–1412.
- (31) Cahn, J. W. Interfacial segregation. *American Society for Metals, Metals Park, Ohio* **1977**,
- (32) Meyer, B. Surface Phase Diagrams from Ab Initio Thermodynamics. *Computational Nanoscience: Do It Yourself* **2006**, *31*, 411–418.
- (33) Christensen, A.; Ruban, A. V.; Stoltze, P.; Jacobsen, K. W.; Skriver, H. L.; Nørskov, J. K.; Besenbacher, F. Phase Diagrams for Surface Alloys. *Phys. Rev. B* **1997**, *56*, 5822–5834.
- (34) Schmidt, W. G.; Mirbt, S.; Bechstedt, F. Surface Phase Diagram of  $(2 \times 4)$  and  $(4 \times 2)$  Reconstructions of GaAs(001). *Phys. Rev. B: Condens. Matter Mater. Phys.* **2000**, *62*, 8087–8091.
- (35) Pilania, G.; Gao, P.-X.; Ramprasad, R. Establishing the LaMnO<sub>3</sub> Surface Phase Diagram in an Oxygen Environment: An ab Initio Kinetic Monte Carlo Simulation Study. *J. Phys. Chem. C* **2012**, *116*, 26349–26357.
- (36) Ito, T.; Akiyama, T.; Nakamura, K. An ab Initio-Based Approach to Phase Diagram Calculations for GaAs(0 0 1)-(2 × 4) $\gamma$  Surfaces. *Appl. Surf. Sci.* **2008**, *254*, 7663–7667.
- (37) Van de Walle, C. G.; Neugebauer, J. First-Principles Surface Phase Diagram for Hydrogen on GaN Surfaces. *Phys. Rev. Lett.* **2002**, *88*, 4.

- (38) Huang, X.; Bennett, J. W.; Hang, M. N.; Laudadio, E. D.; Hamers, R. J.; Mason, S. E. Ab Initio Atomistic Thermodynamics Study of the (001) Surface of LiCoO<sub>2</sub> in a Water Environment and Implications for Reactivity under Ambient Conditions. *J. Phys. Chem. C* **2017**, *121*, 5069–5080.
- (39) Novotny, Z.; Mulakaluri, N.; Edes, Z.; Schmid, M.; Pentcheva, R.; Diebold, U.; Parkinson, G. S. Probing the Surface Phase Diagram of Fe<sub>3</sub>O<sub>4</sub> (001) towards the Fe-Rich Limit: Evidence for Progressive Reduction of the Surface. *Phys. Rev. B: Condens. Matter Mater. Phys.* **2013**, *87*, 1–8.
- (40) Kim, S.; Aykol, M.; Wolverton, C. Surface Phase Diagram and Stability of (001) and (111) LiMn<sub>2</sub>O<sub>4</sub> Spinel Oxides. *Phys. Rev. B: Condens. Matter Mater. Phys.* **2015**, *92*, 7–10.
- (41) Yoo, S. H.; Todorova, M.; Neugebauer, J. Selective Solvent-Induced Stabilization of Polar Oxide Surfaces in an Electrochemical Environment. *Phys. Rev. Lett.* **2018**, *120*, 66101.
- (42) Amirjalayer, S.; Tafipolsky, M.; Schmid, R. Surface Termination of the Metal-Organic Framework HKUST-1: A Theoretical Investigation. *The Journal of Physical Chemistry Letters* **2014**, *5*, 3206–3210, PMID: 26276333.
- (43) Kresse, G.; Hafner, J. Ab Initio Molecular Dynamics for Liquid Metals. *Phys. Rev. B* **1993**, *47*, 558–561.
- (44) Kresse, G.; Hafner, J. Ab Initio Molecular-Dynamics Simulation of the Liquid-Metal–Amorphous-Semiconductor Transition in Germanium. *Phys. Rev. B* **1994**, *49*, 14251–14269.
- (45) Kresse, G.; Furthmüller, J. Efficient Iterative Schemes for Ab Initio Total-Energy Calculations Using a Plane-Wave Basis Set. *Phys. Rev. B* **1996**, *54*, 11169–11186.
- (46) Kresse, G.; Furthmüller, J. Efficiency of Ab-initio Total Energy Calculations for Metals and Semiconductors Using a Plane-Wave Basis Set. *Comput. Mat. Sci.* **1996**, *6*, 15–50.
- (47) Blöchl, P. E. Projector Augmented-Wave Method. *Phys. Rev. B* **1994**, *50*, 17953–17979.
- (48) Joubert, D. From Ultrasoft Pseudopotentials to the Projector Augmented-Wave Method. *Phys. Rev. B* **1999**, *59*, 1758–1775.
- (49) Perdew, J. P.; Burke, K.; Ernzerhof, M. Generalized Gradient Approximation Made Simple. *Phys. Rev. Lett.* **1996**, *77*, 3865–3868.
- (50) Grimme, S.; Antony, J.; Ehrlich, S.; Krieg, H. A Consistent and Accurate Ab Initio Parametrization of Density Functional Dispersion Correction (DFT-D) for the 94 Elements H-Pu. *J. Chem. Phys.* **2010**, *132*, 154104.

- (51) Reuter, K.; Scheffler, M. Composition, Structure, and Stability of RuO<sub>2</sub>(110) as a Function of Oxygen Pressure. *Phys. Rev. B: Condens. Matter Mater. Phys.* **2002**, *65*, 1–11.
- (52) Wolfenden, R.; Liang, Y. L.; Matthews, M.; Williams, R. Cooperativity and Anticooperativity in Solvation by Water: Imidazoles, Quinones, Nitrophenols, Nitrophenolate, and Nitrothiophenolate Ions. *J. Am. Chem. Soc.* **1987**, *109*, 463–466.
- (53) Wagner, W.; Pruß, A. The IAPWS Formulation 1995 for the Thermodynamic Properties of Ordinary Water Substance for General and Scientific Use. *J. Phys. Chem. Ref. Data* **2002**, *31*, 387–535.
- (54) Martínez, L.; Andrade, R.; Birgin, E. G.; Martínez, J. M. PACKMOL: A Package for Building Initial Configurations for Molecular Dynamics Simulations. *J. Comput. Chem.* **2009**, *30*, 2157–2164.
- (55) Weng, T.; Schmidt, J. R. Flexible and Transferable ab Initio Force Field for Zeolitic Imidazolate Frameworks: ZIF-FF. *J. Phys. Chem. A* **2019**, *123*, 3000–3012, PMID: 30835124.
- (56) Horn, H. W.; Swope, W. C.; Pitner, J. W.; Madura, J. D.; Dick, T. J.; Hura, G. L.; Head-Gordon, T. Development of an Improved Four-Site Water Model for Biomolecular Simulations: TIP4P-Ew. *J. Chem. Phys.* **2004**, *120*, 9665–9678.
- (57) Manz, T. A.; Sholl, D. S. Improved Atoms-in-Molecule Charge Partitioning Functional for Simultaneously Reproducing the Electrostatic Potential and Chemical States in Periodic and Nonperiodic Materials. *J. Chem. Theo. Comput.* **2012**, *8*, 2844–2867.
- (58) Manz, T. A.; Limas, N. G. Introducing DDEC6 Atomic Population Analysis: Part 1. Charge Partitioning Theory and Methodology. *RSC Adv.* **2016**, *6*, 47771–47801.
- (59) Plimpton, S. Fast Parallel Algorithms for Short-Range Molecular Dynamics. *J. Comput. Phys.* **1995**, *117*, 1–19.
- (60) Hockney, R.; Eastwood, J. *Computer Simulation Using Particles*; McGraw-Hill, New York, 1981.
- (61) Yang, L.; Huang, K.; Yang, X. Dielectric Properties of N,N-Dimethylformamide Aqueous Solutions in External Electromagnetic Fields by Molecular Dynamics Simulation. *J. Phys. Chem. A* **2010**, *114*, 1185–1190, PMID: 20000563.
- (62) Lide, D. R. *CRC Handbook of Chemistry and Physics*; CRC press, 2004; Vol. 85.
- (63) Tanaka, S.; Fujita, K.; Miyake, Y.; Miyamoto, M.; Hasegawa, Y.; Makino, T.; Van der Perre, S.; Cousin Saint Remi, J.; Van Assche, T.; Baron, G. V. et al. Adsorption and Diffusion Phenomena in Crystal Size Engineered ZIF-8 MOF. *J. Phys. Chem. C* **2015**, *119*, 28430–28439.

- (64) Kida, K.; Okita, M.; Fujita, K.; Tanaka, S.; Miyake, Y. Formation of High Crystalline ZIF-8 in an Aqueous Solution. *CrystEngComm* **2013**, *15*, 1794–1801.
- (65) Avci, C.; Ariñez-Soriano, J.; Carné-Sánchez, A.; Guillerm, V.; Carbonell, C.; Imaz, I.; Maspoch, D. Post-Synthetic Anisotropic Wet-Chemical Etching of Colloidal Sodalite ZIF Crystals. *Angew. Chem., Int. Ed.* **2015**, *54*, 14417–14421.

# Graphical TOC Entry

